

GEOMETRIC AHARONOV–BOHM PHASE EFFECT AROUND A BLACK HOLE

Kaushlendra Kumar and Shahn Majid

School of Mathematical Sciences
Queen Mary University of London
Mile End Road, London E1 4NS, UK

ABSTRACT. In recent work, we have explored the novel possibility that the geodesic of a spacetime density flow in GR could be upgraded to an amplitude ψ with density $|\psi|^2$. We show how this arises from generally-covariant quantum mechanics and the Klein-Gordon operator in a semiclassical analysis, and how it connects to the Raychaudhuri equations. In this setting, we demonstrate an Aharonov–Bohm type effect for the phase of ψ in motion approaching a black hole.

1. INTRODUCTION

Even though the concept of a quantum geodesic was developed with ingredients from noncommutative geometry [4, 5], it can also be applied on ordinary classical manifolds. In a recent work by the authors [14], this idea was studied on a classical black-hole background, using Kruskal–Szekeres coordinates in a spherically reduced system. In its classical limit, the primary object is not a single geodesic $\gamma(s)$, but rather a velocity field $X = X(s, x)$ governing the flow of a local dust of particles with respect to the collective parameter s . The field evolves by the velocity-flow equation

$$\dot{X} + \nabla_X X = 0, \quad (1)$$

where the dot denotes $\partial/\partial s$. Once X is known, it propels any local density $\rho(s)$ by the density-flow equation

$$\dot{\rho} + X(\rho) + \rho \operatorname{div}(X) = 0. \quad (2)$$

The intuition behind these equations was confirmed in [14] as a model of a bunch of geodesics, each with its own parameter s , approximated by corresponding interpolated Gaussian density profiles. In the limiting case of a smooth density of particles over spacetime, s becomes a collective coordinate for the proper time experienced by every particle or observer that moves with the geodesic flow. Due to its noncommutative-geometric origin, however, the same formalism also allows a complex wave-function ψ , via the amplitude-flow equation

$$\dot{\psi} + X(\psi) + \frac{1}{2} \operatorname{div}(X)\psi = 0. \quad (3)$$

Date: May 28, 2026.

2020 Mathematics Subject Classification. Primary 83C65, 83C57, 81S30, 81Q35, 81R50.

Key words and phrases. noncommutative geometry, quantum mechanics, black-holes, quantum spacetime, quantum geodesics, quantum gravity.

Authors to whom correspondence should be addressed: kaushlendra.kumar@qmul.ac.uk and s.majid@qmul.ac.uk.

Funding: KK was supported by a DFG project grant 515782239 and SM by a Leverhulme Trust project grant RPG-2024-177.

This not only implies (2) for $\rho = |\psi|^2$, but contains more information: since the coefficients of the equation are real, the phase of a complex amplitude ψ is transported independently of the modulus. Indeed, whenever $\psi = \sqrt{\rho}e^{i\vartheta}$ is a smooth polar decomposition, the additional information in (3) amounts to

$$\dot{\vartheta} + X(\vartheta) = 0. \quad (4)$$

After setting up this statistical comparison with ordinary geodesics as proof of concept, [14] used Kruskal–Szekeres coordinates (U, V) to study the density and amplitude profiles around a black-hole both outside and crossing through into the interior. The work also gave a first genuine test of the amplitude formalism: two density bumps merge into a single transported bump, while two complex amplitude bumps with opposite relative phase merge to a completely different dipole profile of $|\psi|^2$.

The equations solved in [14] were, however, all in radius-time form with no angular dependence. As a result, we were not placed to demonstrate an Aharonov–Bohm (AB) effect which should be a further outcome of the wave-function hypothesis. To achieve this, we now go one step higher and work in the axially symmetric (U, V, θ) system to ask how the same black-hole geodesic flow transports an initially prepared angular phase. The central theoretical result is the reduced phase law

$$\varphi_k(s, x) = -k \int_0^s X^\theta(\tau, \gamma(\tau)) d\tau, \quad (5)$$

where γ is the backward integral curve of the reduced geodesic velocity field X , ending at the observation point x at flow time s and k is the angular mode number for the θ variable of the spherical polar coordinates of each sphere at a given r, t . This phase law (5) amounts to a geometric AB-type mechanism, but coming from the geometry rather than an electromagnetic solenoid or holonomy as would normally be the case. The mode number k plays the role of a charge, X^θ plays the role of the connection component, and the observable consequence is a shift of an interference profile. We then proceed to numerically illustrate the phase law in two complementary ways. The direct reduced phase extracted from the solved wave-function gives the sharpest internal validation of the phase law. Secondly, a UV -integrated interference ratio $\bar{R}_k(s, \theta)$, built from coherent superpositions, along wave-packet centroid (ψ^2 -weighted packet centre location) provides a more physical intensity-level reading.

We note that geometric and gravitational phase effects are already known in some other contexts. Berry’s phase [9] concerns adiabatic transport in parameter space, while Colella et al.’s neutron experiment [10] and the analyses of Anandan [2] and Stodolsky [21] concern gravitational or inertial phases in matter-wave interference. Closer to the present work are notions of an AB effect in a curved space setting. Early weak-field and global-spacetime versions include Papini’s [18] gravitomagnetic matter-wave phase, Dowker’s [11] construction based on spacetime with nontrivial global topology, Stachel’s [19] globally stationary but locally static space-times, and the spin-connection/mass-current Dirac analogue of Lawrence et al. [15]. More recent matter-wave versions by Hohensee et al. [12] and Overstreet et al. [17] concern gravitational-potential/redshift phases in force-free or near force-free interferometric settings. Our mechanism is novel and different from all of these examples and settings as it pertains to the flow of geodesics in an amplitude form of a wave-function on spacetime with the role of background field played by the angular component X^θ of the geodesic velocity field.

This idea of geodesic flow has deep similarity with fluid mechanics in [3, 6, 5] and discussed in more detail in [14]. For any scalar f or vector field Y one has a

convective derivative with respect to a velocity field X ,

$$\frac{D}{Ds}\Big|_X f = \dot{f} + X(f), \quad \frac{D}{Ds}\Big|_X Y = \dot{Y} + \nabla_X Y.$$

The length and divergence of X obey[5]

$$\frac{D}{Ds}\Big|_X |X|^2 = 0, \quad \frac{D}{Ds}\Big|_X \operatorname{div}(X) = -(\nabla_\mu X^\nu)(\nabla_\nu X^\mu) - R_{\mu\nu} X^\mu X^\nu. \quad (6)$$

The first identity preserves the unit-speed condition while we will show in Appendix B that the second should be understood as the compact version of a convective-Raychaudhuri equation.

Moreover, the works [7] and [14] also looked (in the second case in Kruskal coordinates) at scalar fields ϕ undergoing a flow via the Klein-Gordon operator (so, stationary modes are solutions of the Klein-Gordon equations). In a non-relativistic limit this also leads to a kind of pseudo-quantum mechanics. We show in Appendix A how a complex-envelope expansion of the Klein-Gordon flow indeed gives the above geodesic velocity and amplitude-flow system for the slow envelope, thereby providing for the first time a derivation of (1) and (3) from general relativistic quantum mechanics[7]. The latter in its Heisenberg form involves flows under s of position and momentum operators which in the classical limit become the usual geodesic equations in first order form with s as proper time.

The paper is organised as follows. Section 2 sets up the 4D Schwarzschild–Kruskal flow equations, their axial reduction, and the Ehrenfest identities for the centroid. Section 3 constructs phase-carrying wave-packets, derives the exact solution and the above k -linear reduced phase law, and formulates the interference observable. Section 4 provides the numerical validation: packet transport, direct reduced phase extraction, and the intensity-level phase extraction. Appendices A and B complete the theoretical basis of the framework as discussed above.

2. FLOW EQUATIONS IN 4D SCHWARZSCHILD–KRUSKAL SETTING

This section recaps the geometry of Schwarzschild and Kruskal–Szekeres coordinates and expands the flow equations in the full 4D framework that are to be reduced via axial symmetry in the next section.

2.1. Schwarzschild and Kruskal–Szekeres coordinates. We begin with the Schwarzschild metric in standard coordinates (t, r, θ, ϕ) , with Schwarzschild radius $r_s = 1$,

$$ds^2 = -\left(1 - \frac{1}{r}\right)dt^2 + \left(1 - \frac{1}{r}\right)^{-1}dr^2 + r^2(d\theta^2 + \sin^2\theta d\phi^2). \quad (7)$$

This form suffers from the well-known horizon singularity at $r = 1$, which is nothing but a coordinate artefact.

To describe the geodesic velocity field (and possible wave packet motion) all the way inside horizon without issues, we work instead in Kruskal–Szekeres double-null coordinates (U, V, θ, ϕ) . The extended spacetime, in these coordinates, is divided into four regions separated by the hypersurfaces $U = V = 0$: Region I ($U < 0, V > 0$), the exterior; Region II ($U > 0, V > 0$), the black-hole interior; Region III ($U > 0, V < 0$), the second exterior (interpreted as parallel inaccessible region); and Region IV ($U < 0, V < 0$), the white-hole interior (a time reversed black-hole region where nothing falls in). For our considerations here, the relevant spacetime sector is region-I where the future horizon is $\{U = 0, V > 0\}$ and the past horizon is $\{V = 0, U < 0\}$, as depicted in Figure 1.

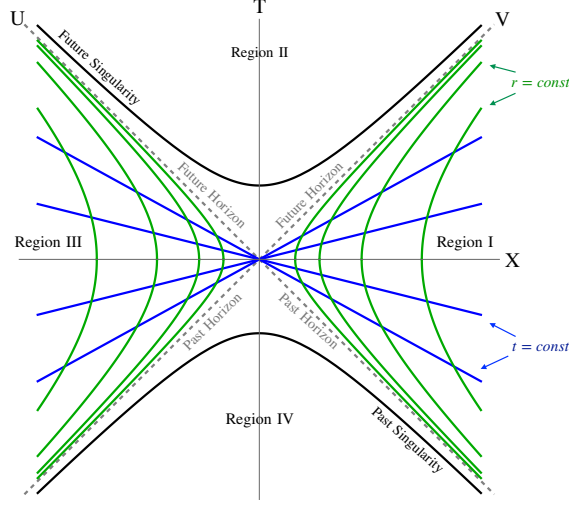


FIGURE 1. Kruskal-Szekeres diagram with various axes and regions marked. The dashed grey lines are the horizons while the black hyperbolae are the singularities. Also, the constant Schwarzschild time/radius slices in the exterior are depicted in blue/green.

More concretely, this is easily seen by introducing the tortoise coordinate and Schwarzschild null coordinates

$$r_* = r + \ln|r - 1|, \quad u = t - r_*, \quad v = t + r_*. \quad (8)$$

In Region I ($U < 0, V > 0$) one may then take

$$U = -e^{-u/2}, \quad V = e^{v/2}, \quad (9)$$

so that one has following global implicit relation valid on all four Kruskal sectors:

$$UV = -(r - 1)e^r, \quad r(U, V) = 1 + W(-UV/e), \quad (10)$$

where W refers to principal Lambert function. In Region I the Schwarzschild time is recovered from the ratio relation

$$t = \frac{1}{2}(v + u) = \ln\left(-\frac{V}{U}\right).$$

The metric in these coordinates is

$$ds^2 = -\frac{4}{r}e^{-r} dU dV + r^2(d\theta^2 + \sin^2\theta d\phi^2), \quad (11)$$

with $g_{UV} = g_{VU} = -\frac{2}{r}e^{-r}$, so that $\sqrt{-g} = 2re^{-r} \sin\theta$. Unlike the Schwarzschild metric (7), this one is C^∞ -regular at, e.g. the future horizon $U = 0$ corresponding to $r = 1$.

The non-zero Christoffel symbols of the metric (11) are given explicitly as,

$$\begin{aligned} \Gamma_{UU}^U &= \frac{r+1}{r^2}Ve^{-r}, & \Gamma_{\theta\theta}^U &= -\frac{Ur}{2}, & \Gamma_{\phi\phi}^U &= -\frac{Ur}{2}\sin^2\theta, \\ \Gamma_{VV}^V &= \frac{r+1}{r^2}Ue^{-r}, & \Gamma_{\theta\theta}^V &= -\frac{Vr}{2}, & \Gamma_{\phi\phi}^V &= -\frac{Vr}{2}\sin^2\theta, \\ \Gamma_{U\theta}^\theta &= -\frac{e^{-r}}{r^2}V, & \Gamma_{V\theta}^\theta &= -\frac{e^{-r}}{r^2}U, & \Gamma_{\phi\phi}^\theta &= -\sin\theta \cos\theta, \\ \Gamma_{U\phi}^\phi &= -\frac{e^{-r}}{r^2}V, & \Gamma_{V\phi}^\phi &= -\frac{e^{-r}}{r^2}U, & \Gamma_{\theta\phi}^\phi &= \cot\theta, \end{aligned} \quad (12)$$

with $r = r(U, V)$ understood throughout.

2.2. Full 4D geodesic velocity and amplitude-flow equations. The geodesic velocity equation (1) in local coordinates $x^\alpha = (U, V, \theta, \phi)$ reads

$$\dot{X}^\alpha + X^\beta \partial_\beta X^\alpha + \Gamma_{\beta\rho}^\alpha X^\beta X^\rho = 0, \quad \alpha \in \{U, V, \theta, \phi\}. \quad (13)$$

Using the Christoffel symbols (12), the four component equations are

$$\dot{X}^U + X^\beta \partial_\beta X^U + \frac{r+1}{r^2} V e^{-r} (X^U)^2 - \frac{Ur}{2} [(X^\theta)^2 + \sin^2 \theta (X^\phi)^2] = 0, \quad (14)$$

$$\dot{X}^V + X^\beta \partial_\beta X^V + \frac{r+1}{r^2} U e^{-r} (X^V)^2 - \frac{Vr}{2} [(X^\theta)^2 + \sin^2 \theta (X^\phi)^2] = 0, \quad (15)$$

$$\dot{X}^\theta + X^\beta \partial_\beta X^\theta - \frac{2e^{-r}}{r^2} (UX^V + VX^U) X^\theta - \sin \theta \cos \theta (X^\phi)^2 = 0, \quad (16)$$

$$\dot{X}^\phi + X^\beta \partial_\beta X^\phi - \frac{2e^{-r}}{r^2} (UX^V + VX^U) X^\phi + 2 \cot \theta X^\theta X^\phi = 0. \quad (17)$$

Moreover, the unit-speed condition $|X|^2 = -1$, preserved by (1), reads

$$-\frac{4}{r} e^{-r} X^U X^V + r^2 [(X^\theta)^2 + \sin^2 \theta (X^\phi)^2] = -1. \quad (18)$$

The associated amplitude-flow equation for a complex scalar field $\psi(s, x)$ is

$$\dot{\psi} + X^\alpha \partial_\alpha \psi + \frac{1}{2} \operatorname{div}(X) \psi = 0, \quad (19)$$

where the full four-dimensional covariant divergence in Kruskal variables is

$$\operatorname{div}(X) = \partial_\alpha X^\alpha + \frac{r-1}{r^2} e^{-r} (VX^U + UX^V) + \cot \theta X^\theta. \quad (20)$$

For the geometric-phase analysis below we restrict the above 4D flow system to the axially symmetric case with θ angular-mode wave-packets.

2.3. Axial reduction of the full 4D system. We now specialize the full 4D flow equations to the axially symmetric case that will then be used in the geometric-phase calculation in the later sections.

$$X^\phi \equiv 0, \quad \partial_\phi \equiv 0$$

for all fields. This is the natural setting for the angular-mode initial data $e^{ik(\theta-\theta_0)}$ used below. Setting $X^\phi = 0$ in (17) is consistent (remains true during evolution), while the remaining three equations (14)-(16) reduce to

$$\dot{X}^U + X^\mu \partial_\mu X^U + \frac{r+1}{r^2} V e^{-r} (X^U)^2 - \frac{Ur}{2} (X^\theta)^2 = 0, \quad (21)$$

$$\dot{X}^V + X^\mu \partial_\mu X^V + \frac{r+1}{r^2} U e^{-r} (X^V)^2 - \frac{Vr}{2} (X^\theta)^2 = 0, \quad (22)$$

$$\dot{X}^\theta + X^\mu \partial_\mu X^\theta - \frac{2e^{-r}}{r^2} (UX^V + VX^U) X^\theta = 0, \quad (23)$$

where, from now on

$$x^\mu = (U, V, \theta), \quad X = X^\mu \partial_\mu, \quad \mu, \nu \in \{U, V, \theta\}. \quad (24)$$

This is the notation used throughout the rest of the paper. The reduced unit-speed condition is

$$-\frac{4}{r} e^{-r} X^U X^V + r^2 (X^\theta)^2 = -1. \quad (25)$$

The reduced amplitude-flow equation is

$$\dot{\psi} + X^\mu \partial_\mu \psi + \frac{1}{2} \operatorname{div}(X) \psi = 0, \quad (26)$$

with reduced covariant divergence

$$\operatorname{div}(X) = \partial_\mu X^\mu + \frac{r-1}{r^2} e^{-r} (V X^U + U X^V) + \cot \theta X^\theta. \quad (27)$$

2.4. Covariant continuity equation and conserved mass. The amplitude flow equation can be reformulated into a continuity equation for density

$$\rho(s, x) := |\psi(s, x)|^2.$$

To see this, multiply (26) by ψ^* , add the complex conjugate, and use the reality of X to get

$$\dot{\rho} + \nabla_\mu(\rho X^\mu) = 0. \quad (28)$$

This naturally leads to a notion of conserved total mass (provided the boundary flux vanishes) for evolving wave-function, given by

$$N(s) := \int_M \rho(s, x) d\mu, \quad (29)$$

where the measure is over the full 4D spacetime manifold M , so in our case

$$d\mu = 4\pi r e^{-r} \sin \theta dU dV d\theta. \quad (30)$$

This is the basic conservation law behind the centroid diagnostics used later.

2.5. Ehrenfest identities for centroid transport. For any smooth scalar observable $f = f(s, x)$, we can define its expectation value as

$$\langle f \rangle(s) := \frac{1}{N} \int_M f(s, x) \rho(s, x) d\mu. \quad (31)$$

Differentiating with respect to s , using (28), and integrating by parts on the manifold gives the following Ehrenfest identity

$$\frac{d}{ds} \langle f \rangle = \langle \dot{f} + X(f) \rangle \quad (32)$$

This is nothing but the convective transport,

$$D_X f := \frac{D}{Ds} \Big|_X f = \dot{f} + X(f) = \partial_s f + X^\nu \partial_\nu f$$

of the scalar observable f . The centroid transport equations follow immediately by taking $f = U, V, \theta$:

$$\frac{d\langle U \rangle}{ds} = \langle X^U \rangle, \quad \frac{d\langle V \rangle}{ds} = \langle X^V \rangle, \quad \frac{d\langle \theta \rangle}{ds} = \langle X^\theta \rangle. \quad (33)$$

These are the precise mathematical justification for using the packet centroid in numerical diagnostics below, as they follow the averaged geodesic velocity field.

Applying (32) to the s -dependent observable $f = X^\mu$ then gives

$$\frac{d^2 \langle x^\mu \rangle}{ds^2} = \langle D_X X^\mu \rangle, \quad (34)$$

which is the exact second-order Ehrenfest relation. Using the geodesic velocity equation (13) componentwise,

$$D_X X^\mu = \partial_s X^\mu + X^\nu \partial_\nu X^\mu = -\Gamma_{\nu\sigma}^\mu X^\nu X^\sigma,$$

we have the equivalent version:

$$\frac{d^2 \langle x^\mu \rangle}{ds^2} = -\langle \Gamma_{\nu\sigma}^\mu X^\nu X^\sigma \rangle \approx -\Gamma_{\nu\sigma}^\mu(\bar{x}) \langle X^\nu \rangle \langle X^\sigma \rangle. \quad (35)$$

Here, $\bar{x} = \langle x \rangle$ is the centroid location, and the approximation is in the narrow-packet limit, where the density ρ is sharply concentrated near the centroid \bar{x} and variations of both Christoffel and velocity terms are negligible across packets. Thus,

in this particle-like regime, the centroid itself approximately obeys the ordinary geodesic equation.

3. FRAMEWORK FOR GEOMETRIC AHARONOV–BOHM PHASE

We will work in the reduced system (2.3) with U, V, θ as coordinates. The first step is the construction of a suitable geodesic velocity field X . Then we discuss the wave-packet form of ψ as well as the notion of backward integral curves ending at chosen observation points. This leads to a phase formula which will be used in the numerical analysis in Section 4.

3.1. Construction of the geodesic velocity field. The initial geodesic velocity field at $s = 0$ is constructed by starting from a 2D field in the (U, V) sector and then lifting it into the current 3D setting. The 2D fields with components $\tilde{X} = (\tilde{X}^U(U, V), \tilde{X}^V(U, V))$, are required to satisfy two conditions as in [14],

$$\partial_U \tilde{X}^U + \partial_V \tilde{X}^V + \frac{r-1}{r^2} e^{-r} (V \tilde{X}^U + U \tilde{X}^V) = 0, \quad -\frac{4}{r} e^{-r} \tilde{X}^U \tilde{X}^V = -1. \quad (36)$$

The first is the 2D covariant divergence-free condition $\text{div}(\tilde{X}) = 0$ and the second is the Lorentzian unit-speed condition $|\tilde{X}|^2 = -1$ in the (U, V) -sector. Solving the second for \tilde{X}^V gives

$$\tilde{X}^V = \frac{r e^r}{4 \tilde{X}^U}, \quad (37)$$

reducing the first to a single second-order PDE for \tilde{X}^U , solved numerically with Dirichlet data $\tilde{X}^U|_{U_{\min}} = 5$ on the inflow face $U_{\min} = -4$, providing an ingoing flow. We then choose the initial 3D data at $s = 0$ as

$$\begin{aligned} X^U(0, U, V, \theta) &= \tilde{X}^U(U, V) \sqrt{1 + r(U, V)^2 \sin^2 \theta}, \\ X^V(0, U, V, \theta) &= \tilde{X}^V(U, V) \sqrt{1 + r(U, V)^2 \sin^2 \theta}, \\ X^\theta(0, U, V, \theta) &= \sin \theta, \end{aligned} \quad (38)$$

which, owing to (36), satisfies the 3D unit-speed condition (25) and restricts to \tilde{X} at the poles $\theta = 0, \pi$. These 3D fields also preserve the U, V symmetry of the system. Furthermore, the choice $X^\theta(0) = \sin \theta$ ensures that the field vanishes at the poles of the unit-sphere.

Once the initial velocity fields have been specified as above, the full field $X(s, U, V, \theta)$ is obtained for $s > 0$ by numerically evolving the geodesic velocity equations (21)–(23). Throughout the rest of the paper we work in Region I on the domain

$$U \in [-4, -0.1], \quad V \in [0.1, 6], \quad \theta \in [0.05, \pi - 0.05], \quad (39)$$

where the safe angular cut-off 0.05 keeps the amplitude-flow equation away from the coordinate singularities at the two poles. We solve the PDE system using `NDSolve` of Mathematica using the `MethodOfLines` for s with `FiniteElements` for (U, V, θ) and grid-cell resolution `res = MaxCellMeasure = 0.005`, while fixing $X = X(0)$ at the $U_{\min} = -4$ boundary. The angular component X^θ , that appears in the geometric phase formula (48), is positive throughout the specified part of Region I. We illustrate the resulting fields $X^U(s)$ and $X^V(s)$ thus obtained with $V = 3$ slices at $s = 0, 0.15, 0.3$ in Figure 2. The plots for $X^V(s)$ are similar to that of $X^U(s)$ so we refrain from showing those here.

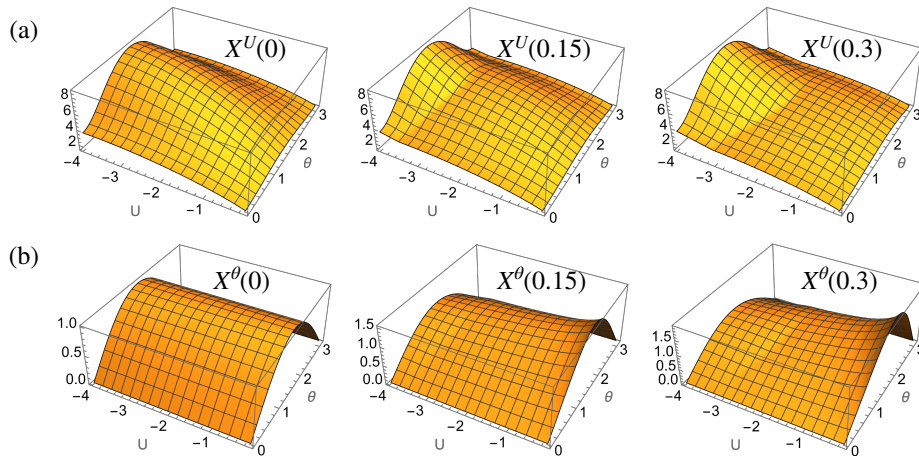


FIGURE 2. Plots of velocity field at $s = 0, 0.15, 0.3$ shown for components (a) $X^U(s)$ and (b) $X^\theta(s)$.

3.2. Wave-packets carrying the phase. We next consider initial data for the numerical runs for ψ_k as a 3D Gaussian wave-packet centred at (U_0, V_0, θ_0) with the same width σ along all three coordinates,

$$\psi_k(0, U, V, \theta) = G(U, V, \theta) e^{ik(\theta - \theta_0)}, \quad (40)$$

where the Gaussian envelope is k -independent and given by

$$G(U, V, \theta) = \exp\left[-\frac{(U - U_0)^2 + (V - V_0)^2 + (\theta - \theta_0)^2}{2\sigma^2}\right]. \quad (41)$$

For the mode number k , we focus the numerical analysis below in three of them:

$k = 0$	reference envelope mode, used to isolate amplitude transport,
$k = 2$	main interference mode together with $k = 0$ mode,
$k = 4$	higher-mode confirmation of exact k -linearity.

The case $k = 1$ can also be computed, but the shift is more visible for $k = 2$ and higher. As the wave-packet (40) evolves according to the amplitude flow (26), it is transported and deformed by the flow. A natural way to track the packet motion is through the centroid, namely the averaged position weighted by $|\psi|^2$, whose evolution is governed by the Ehrenfest identities discussed in Section 2.5. This is the usual wave-packet viewpoint, in which a localised packet is compared with a centre or reference trajectory and the deformation of nearby support [16]. For the phase law, however, the more precise object is the backward integral curve of the vector field X ending at the chosen observation point at time s . The observation point may be taken to be the centroid, but the backward integral curve need not retrace the centroid path exactly; the mismatch gets smaller with narrow packets.

3.3. Backward integral curves and exact solution. For a fixed point $x^\mu = (U, V, \theta)$ at flow time s , we define $\gamma^\mu(\tau)$ to be the backward integral curve ending at x^μ at time s , characterised by

$$\dot{\gamma}^\mu(\tau) = X^\mu(\tau, \gamma(\tau)), \quad \gamma^\mu(s) = x^\mu, \quad \tau \leq s. \quad (42)$$

Now for any smooth function $f(\tau, x)$ we have,

$$\begin{aligned} \frac{d}{d\tau} f(\tau, \gamma(\tau)) &= \frac{\partial f}{\partial \tau}(\tau, \gamma(\tau)) + \dot{\gamma}^\mu(\tau) \partial_\mu f(\tau, \gamma(\tau)) \\ &= \frac{\partial f}{\partial \tau}(\tau, \gamma(\tau)) + X^\mu(\tau, \gamma(\tau)) \partial_\mu f(\tau, \gamma(\tau)). \end{aligned}$$

Applying this to $f = \psi$ and using (26), we obtain

$$\begin{aligned} \frac{d}{d\tau} \psi(\tau, \gamma(\tau)) &= (\partial_\tau + X^\mu \partial_\mu) \psi(\tau, \gamma(\tau)) \\ &= -\frac{1}{2} \operatorname{div}(X)(\tau, \gamma(\tau)) \psi(\tau, \gamma(\tau)). \end{aligned}$$

Integrating this scalar ODE along γ gives the exact solution

$$\psi(s, x) = \psi(0, \gamma(0)) \exp\left(-\frac{1}{2} \int_0^s \operatorname{div}(X)(\tau, \gamma(\tau)) d\tau\right). \quad (43)$$

Since $\operatorname{div}(X)$ is real, the exponential factor is real and positive, hence the phase of $\psi(s, x)$ is exactly the initial phase evaluated at the foot $\gamma(0)$. We label the foot of the backward integral curve by

$$x_f := \gamma(0) = (U_f, V_f, \theta_f).$$

Before moving further, it is important to distinguish two distinct angular quantities entering our analysis:

- θ_0 is the *fixed angular reference* built into the initial data (40). It is the angular centre of the initial Gaussian blob and as such is a constant.
- $\theta_f = \theta_f(s, x)$ is the *foot-point angle*, a dynamical quantity obtained by back-tracing the integral curve γ which at flow time s lands at $x = (U, V, \theta)$.

With this distinction established, we can now integrate the θ -component of (42),

$$\theta_f(s, x) = \theta - \int_0^s X^\theta(\tau, \gamma(\tau)) d\tau. \quad (44)$$

Hence the net transported angular displacement relative to the fixed initial reference angle θ_0 is

$$\Delta\theta(s, x) := \theta_f(s, x) - \theta_0 = (\theta - \theta_0) - \int_0^s X^\theta(\tau, \gamma(\tau)) d\tau. \quad (45)$$

3.4. Phase formula and exact k -linearity. For the initial data (40) with $G > 0$ real and independent of k , the exact solution (43) gives

$$\psi_k(s, x) = G(\gamma(0)) e^{ik(\theta_f - \theta_0)} F(s, x),$$

where $\gamma(0) = x_f$ is the foot-point noted above and

$$F(s, x) = \exp\left(-\frac{1}{2} \int_0^s \operatorname{div}(X)(\tau, \gamma(\tau)) d\tau\right) > 0.$$

Note that the modulus is independent of k :

$$|\psi_k(s, x)| = A(s, x) := G(\gamma(0)) F(s, x). \quad (46)$$

The full phase is $k(\theta_f - \theta_0) = k\Delta\theta(s, x)$, so using (45) it splits as

$$\arg \psi_k(s, x) = k(\theta - \theta_0) + \varphi_k(s, x), \quad (47)$$

where the reduced phase encoding the observable shift during the flow is

$$\varphi_k(s, x) := \arg(\psi_k(s, x) e^{-ik(\theta - \theta_0)}) = -k \int_0^s X^\theta(\tau, \gamma(\tau)) d\tau. \quad (48)$$

We will be using this precise phase quantity in Section 4 to compare against the observable phase-shift of the numerical $\psi(s, x)$ data obtained through the flow equation (26). An important point to note here is the exact k -linearity relation in the above phase formula; any deviation noted in Section 4 should be treated as purely numerical error. Finally, one may note that Gaussian envelope G (41) depends on θ alongside (U, V) , but this dependence enters only through $|\psi(s, x)|$ and hence does not play any role in the phase-shift analysis below.

3.5. Interference observable. Having established the geometric setting for the wave-packet evolution and the exact phase law, we now look at how this will be detected through observation of the intensity $|\psi_k|^2$. We consider coherent two-mode superpositions

$$\psi_{0k} := \psi_0 + \psi_k = \psi_0(1 + e^{ki\Delta\theta}).$$

Using (46), we have the pure cross-term

$$|\psi_{0k}|^2 - |\psi_0|^2 - |\psi_k|^2 = 2|\psi_0||\psi_k| \cos(k\Delta\theta). \quad (49)$$

We then use (49) to obtain the observable phase shift from the normalised interference cross-term as

$$\begin{aligned} \bar{R}_k(s, \theta) &= \frac{N_k(s, \theta)}{D_k(s, \theta)}, \\ N_k(s, \theta) &= 2 \int (|\psi_{0k}|^2 - |\psi_0|^2 - |\psi_k|^2) r e^{-r} dU dV, \\ D_k(s, \theta) &= 4 \int |\psi_0||\psi_k| r e^{-r} dU dV. \end{aligned} \quad (50)$$

In the ideal equal-envelope regime $|\psi_0| = |\psi_k|$, (50) that we are interested in, this should reduce to

$$\bar{R}_k = \cos(k\Delta\theta)$$

since this is also the local ratio at each point of U, V . Integrating as we do is better adapted to a packet drifting in the null coordinates (U, V) , since the numerator and denominator are first integrated over the packet support before taking the ratio, removing some of the numerical noise. However, as the ψ_k are evolved separately as a test of data integrity, \bar{R}_k won't exactly have this form due to numerical errors in the numerical evolution. We also have an issue when D_k is small as will see later.

The ideal peak position $\bar{R}_k = 1$ occurs at $\theta_*(s)$, satisfying $\Delta\theta(s, \theta_*) = 2\pi n/k$ for integer n . Note that the packet used in the PDE runs in Section 4 occupies only a small angular window around the original centre: $\theta_0 \pm 2\sigma$ with $\sigma = 0.15$ means $4\sigma_\theta = 0.6$ is only about 38% of the half-period $\pi/2 \approx 1.57$ of $\cos(2\Delta\theta)$. For $k = 4$, the corresponding half-period is $\pi/4 \approx 0.785$, so the same packet spans a larger fraction of the local fringe leading to a narrower principal profile. In both cases the observed phase shift is read from the principal interference feature

$$\varphi_k^{\bar{R}}(s) := -(\theta_*^{(k)}(s) - \theta_0) = \frac{\varphi_k(s)}{k}. \quad (51)$$

Here $\varphi_k(s)$ is the reduced phase from (48), while $\varphi_k^{\bar{R}}$ is the normalised intensity-level phase read from the interference profile.

3.6. Summary of Aharonov–Bohm analogy. We can now summarize the precise sense in which the mechanism is AB-like. The analogy is not gauge-theoretic: there is no electromagnetic vector potential and no ordinary solenoid-type holonomy. Rather, the analogy is at the level of phase accumulation and interference readout. The angular mode number k plays the role of a charge, the velocity

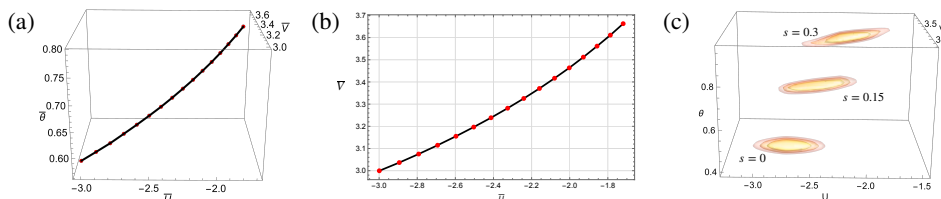


FIGURE 3. Plots showing wave-packet transport with (a) 3D centroid trajectory, (b) 2D projection on centroid trajectory on (U, V) plane and (c) density $\rho(s)$ level-surfaces at $s = 0, 0.15, 0.3$.

component X^θ drives the accumulated phase, and the observable signature is a displacement of the interference profile. The correspondences are:

AB effect	Geodesic velocity field
Charge q	Angular mode number k
Vector potential A_μ	Velocity component X^θ
Line integral $\oint A \cdot dl$	$\int_0^s X^\theta(\tau, \gamma(\tau)) d\tau$
Inaccessible solenoid	Black-hole interior
Observable: interference shift	$\bar{R}_k(\theta, s)$ peak shift

Thus the effect is AB-like at the level of interference structure, but its phase is generated by geodesic transport in the amplitude-flow equation rather than by a gauge potential.

4. NUMERICAL SETUP AND RESULTS

We now test the phase law numerically using the axially reduced system of Section 2.3, the reduced phase formula of Section 3.4, and the interference based phase extraction of Section 3.5. The numerical work has three parts: first we check that the packet remains localised while being transported by the computed geodesic velocity field, followed by the computation of the reduced phase directly from the solved wave-functions and finally the extraction of the corresponding intensity-level phase from the fitted interference profile centre of the UV -integrated ratio \bar{R}_k .

The geodesic velocity field $X(s, U, V, \theta)$ constructed in Section 3.1 is used as a fixed transport background for the ψ -evolution. However, before proceeding, we first sample the velocity field X and its divergence $\text{div}(X)$ on a coarser grid of size 0.05 to speed up the computation, without affecting the overall velocity profiles. Using this interpolation, we solve the amplitude flow equation (26) for the angular wave-packet data (40)-(41) for five different cases, ψ_k, ψ_{0k} with $k = 0, 2, 4$, as explained in Section 3.5. Like before in solving for X , we use Mathematica's NDSolve with the MethodOfLines for s , with FiniteElements for (U, V, θ) and the same spatial resolution scale $\text{MaxCellMeasure} = 0.005$. A Dirichlet condition is imposed only on the inflow boundary $U_{min} = -4$. Although we ran the evolution of these ψ to get raw data till $s = 0.4$, we present the phase comparisons below for $0.05 \leq s \leq 0.30$, since at later times boundary effects become visible.

4.1. Packet motion and numerical checks. We first analyze the packet motion itself in Figure 3 showing the transported centroid,

$$\bar{x}(s) = (\bar{U}(s), \bar{V}(s), \bar{\theta}(s)), \quad (52)$$

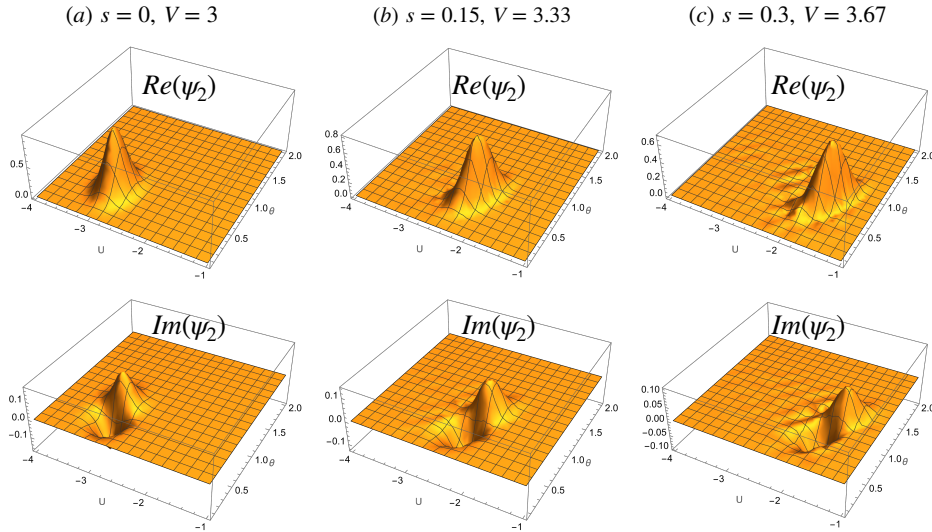


FIGURE 4. Plots showing evolution of wave-function $\psi_2(s)$ at $s = 0, 0.15, 0.3$ and sliced at corresponding centroid values of V .

its projection to the (U, V) -plane and density level-surfaces for the $k = 0$ packet with level-values $(0.6, 0.7, 0.8)$. The centroid moves towards the $U = 0$ horizon with increasing V and θ , in agreement with the positive angular component X^θ of the velocity field. We show the complex amplitude of ψ_2 itself in Figure 4 on slices at the centroid value $V = \bar{V}(s)$ as it evolves in s , this being where the real and imaginary parts remain localised. The ripples visible at later times (i.e., column (c)) are numerical noise from the evolution. The corresponding plots for ψ_0 (always real) and ψ_4 are similar.

To estimate the numerical accuracy we monitor the mass $N(s)$ (29) and find that for single-modes $k = 0, 2, 4$ these remain conserved to within 10^{-3} . We also directly verify that the independently evolved interference fields ψ_{0k} remain linearly related in the correct manner, in that the residual

$$\mathcal{E}_{0k}(s) := \int |\psi_{0k}(s) - \psi_0(s) - \psi_k(s)|^2 d\mu, \quad k = 2, 4,$$

stays within 10^{-6} – 10^{-5} during the evolution. Similarly the amplitudes of individual wave-functions ψ_k match to similar high accuracy, thereby showing phase-independent amplitude evolution (43). Thus the evolutions are stable and free from issues such as non-linearity of interference, mass drift, etc meaning that larger numerical discrepancies below in phase analysis can be attributed to finite-resolution or other numerical effects.

4.2. Direct reduced phase extraction. We first evaluate the reduced phase directly from the above obtained wave-functions by evaluating (48) along the transported centroid (52):

$$\varphi_k^\psi(s) = \arg \left[\psi_k(s, \bar{x}(s)) e^{-ik(\bar{\theta}(s) - \theta_0)} \right].$$

This is compared with the flow prediction $\varphi_k(s)$ given by (5) along the corresponding backward integral curve, evaluated numerically (point-wise evaluations at $\delta s = 0.02$ intervals via a trapezoidal rule along the centroid, followed by interpolation). Figure 5 compares the $k = 2$ and $k = 4$ extracted phases with their flow predictions, and also shows the numerical ratio $\varphi_4^\psi / (2\varphi_2^\psi)$. This ratio tests

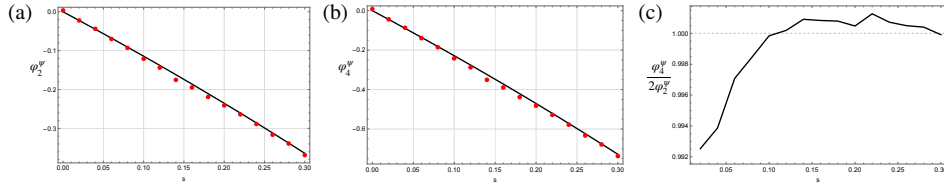


FIGURE 5. Comparison plots of direct reduced phases $\varphi_k^\psi(s)$ against the flow prediction $\varphi_k(s)$ obtained from the velocity field component $X^\theta(s)$ for (a) $k = 2$ and (b) $k = 4$. The normalised ratio $\frac{\varphi_4^\psi}{2\varphi_2^\psi}(s)$ in (c) stays close to 1 as an integrity check of linearity of the phase law.

the exact k -linearity relation by showing that this remains close to 1 during the evolution (slightly low initial values are due to an onset effect for a phase-difference starting from zero). Therefore, this direct wave-function-level extraction offers a sharp numerical validation of the geometric phase law.

4.3. Phase extraction from intensity profiles. As discussed in Section 3.5, the ratio of (U, V) -integrated cross-term N_k and overlap-term D_k provides a more physically meaningful way of extracting the phase, since intensities are closer to laboratory readouts than the complex wave-function itself. However, this ratio is also more delicate computationally because of the denominator overlap integrals that can sometimes become too small and produce artefacts. Keeping this in mind, we obtain this ratio \bar{R}_k (50) through post-processing of the solved fields ψ_k where sampling is done on a grid of size $\delta s = 0.02$ and $\delta\theta = 0.005$. At each s , the raw profile is sampled in a packet-tracking angular window $\bar{\theta}(s) \pm 0.35$ to capture large enough dynamic intervals and record the raw data $(s, \theta, \bar{R}_k, D_k)$.

We then apply some natural filtering on this data to remove the far-tail of the profiles as well as bad sample points. More specifically, for each s -slice we work in a fixed angular band $0.35 \leq \theta \leq 0.95$, discarding points with $D_k \leq 10^{-3}$, and applying a range-filter $0.80 \leq \bar{R}_k \leq 1.03$. We then fit a low-degree curve,

$$\hat{R}_k(s, \theta) = a_0 + a_1\theta + a_2\theta^2 + a_3\theta^3 + a_4\theta^4,$$

of degree at most four on the filtered data. The fitted peak $\theta_*^{(k)}(s)$ defines the normalised intensity-level phase $\varphi_k^{\bar{R}}(s)$ as in (51). Representative sampled profiles

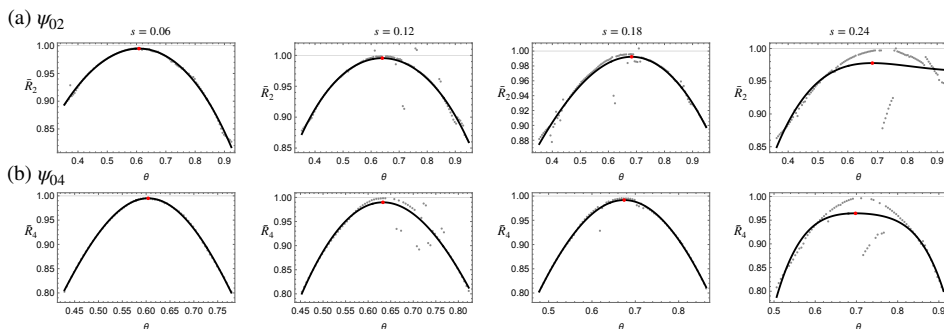


FIGURE 6. Plots of \bar{R}_k sample data, fitted low degree curve and peak location (red dot) at $s = 0.06, 0.12, 0.18, 0.24$ for the interference profiles (a) ψ_{02} , and (b) ψ_{04} .

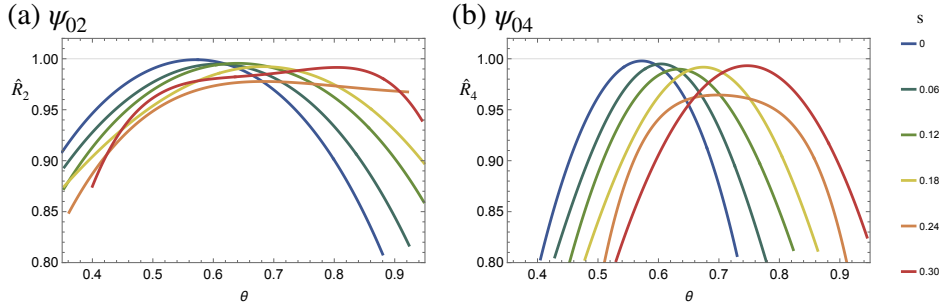


FIGURE 7. Evolution of the fitted interference profiles $\widehat{R}_k(s, \theta)$ for (a) $k = 2$ and (b) $k = 4$. We show reconstructed fitted-curve snapshots at $s = 0, 0.06, 0.12, 0.18, 0.24, 0.3$.

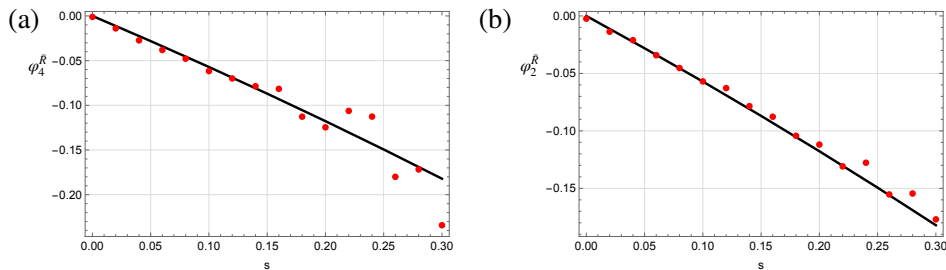


FIGURE 8. Fitted intensity-level phase $\varphi_k^{\widehat{R}}$ compared with the normalised flow prediction φ_k/k .

and fitted curves are shown in Figure 6, the fitted-profile evolution is shown in Figure 7, and the resulting phase comparison with $\varphi_k(s)/k$ is shown in Figure 8. We have also shown the sampled points alongside the fitted curve, showing the presence of a few numerically sensitive outlier points as well as more systematic late-time distortions (peak flattening), especially after about $s \simeq 0.22$, due to erratic denominator D_k values. This explains why a fitted centre is more accurate than trying to find maximum from the raw data itself.

The $k = 2$ profile in Figure 7 (a) is broader compared to the $k = 4$ profile in part (b) because $\cos(k\Delta\theta)$ varies more rapidly with θ for the latter. Compared to the previous direct phase comparison, the ratio-based extraction in this section is more sensitive to numerical errors in the evolution of the different $\psi_0, \psi_k, \psi_{0k}$. In particular, resulting small or uneven values of D_k and late-time flattening can move the fitted maxima. The fitted-centre procedure reduces this sensitivity, and the narrower $k = 4$ profiles give slightly cleaner peak locations as evident from Figure 8(b).

5. CONCLUSION

In this work we have extended the time-radial analysis of geodesic flows around a black hole in [14] to include the angular coordinate θ (the angle from the vertical axis), while assuming symmetry (i.e. ϕ -independence) about the axis. Each dimension added makes the numerical integrations less tractable so only allowed variation in θ . This was enough, however, to demonstrate a novel geometric AB effect under the hypothesis of complex amplitudes underlying matter densities on spacetime. We first set up a geodesic velocity field (38) which has a certain $U - V$ profile at

the poles but in between the poles ‘bulges’ to largest values at the equator as can be seen in Figure 2.

We then looked at initial wave-packet wave-functions ψ_k with phase corresponding to frequency k in the θ direction and density centred as a ‘Gaussian bump’ at some (U_0, V_0, θ_0) . In our case small θ_0 , so including the axial symmetry we have a kind of ring around the vertical axis. We then evolved everything to later s . The centroid angle increases as the ‘ring’ approaches the black hole and we saw how the phases evolve and how their interference evolves. In principle one could continue evolving past the black-hole to centroid values beyond $\pi/2$ but one would need to overcome some numerical issues arising from close to the horizon. The theoretical analysis led to a formula (48) for the phase shift of wave packet which we interpreted in terms of the interference of a linear combination with ψ_0 . The theoretical values were then computed for the case of interest as well as directly for the numerical evolutions with a good match well above numerical noise levels. Although not an actual experiment, the analysis shows a theoretical prediction backed by numerical modelling.

The appendices contain further insights on the theory of quantum geodesic flows on spacetime. We show that these flow equations in fact arise naturally from generally covariant quantum mechanics recently introduced in [7] and that the convective derivative $\text{div}(X)$ of a geodesic velocity field found in [5] involving the Ricci curvature can be viewed as a version of the Raychaudhuri equations in relativistic fluid mechanics.

Overall, we find that the hypothesis that in some contexts the density in relativistic fluid mechanics could be replaced by an underlying spacetime wave-function amplitude leads to new interference effects (of an AB-type). Moreover, the framework we use is now shown to arise naturally from a recent formulation of generally covariant quantum mechanics [7] introduced in both Heisenberg form and in Schrödinger form where it corresponds to a Klein-Gordon flow. Both have been studied around a black-hole[7, 14] and in FLRW backgrounds[8]. As a result, while matters of physical interpretation need to be further explored due to the novel nature of this approach, it appears that there is a natural theoretical basis and the possibility to compute examples, both of which should be developed further. In this respect, other background spacetimes could be studied. A useful next step would be to recast the geodesic family studied in [14] into standard congruence language, including comoving/Lemaître-type frames, expansion, shear, vorticity and caustics in the sense of Appendix B. This should clarify how the present amplitude flow mechanism relates to the ADM lapse-shift description of the same black-hole geometry. Also to be developed further is the adaptation of ideas from relativistic fluid mechanics to the amplitude setting as again suggested by the present work. These are some directions for further work.

APPENDIX A. SEMICLASSICAL KG-ENVELOPE ORIGIN OF THE FLOW

We demonstrate here how to obtain the flow system (1-3) as the leading complex-envelope semiclassical system associated with the Klein–Gordon flow studied previously [7, 14]. This is also needed to fix the distinction between the fast eikonal phase and the slow envelope phase used in the geometric-phase analysis in the main part of the paper.

To this end, we start from the Klein–Gordon flow on spacetime wave-functions $\Phi \in L^2(M)$ [7, 14],

$$-i\hbar \dot{\Phi} = \frac{\hbar^2}{2m} \square \Phi. \quad (53)$$

We now use the complex-envelope WKB/eikonal ansatz

$$\Phi(s, x) = \psi(s, x)e^{iS(s, x)/\hbar}, \quad (54)$$

where S is a real rapidly varying phase and ψ is a slowly varying *complex* envelope. This eikonal phase S should not be confused with phase ϑ of the slow envelope ψ which gets convectively transported by (4).

Since Φ is a scalar, one simply has

$$\dot{\Phi} = e^{iS/\hbar} \left(\dot{\psi} + \frac{i}{\hbar} \psi \dot{S} \right), \quad \nabla_\mu \Phi = \partial_\mu \Phi = e^{iS/\hbar} \left(\nabla_\mu \psi + \frac{i}{\hbar} \psi \nabla_\mu S \right), \quad (55)$$

where a second covariant derivative on the second part gives

$$\square \Phi = e^{iS/\hbar} \left(\square \psi + \frac{2i}{\hbar} \nabla^\mu S \nabla_\mu \psi + \frac{i}{\hbar} (\square S) \psi - \frac{1}{\hbar^2} (\nabla S)^2 \psi \right). \quad (56)$$

Substituting this result for the box operator on Φ along with the first part of (55) into (53) yields,

$$\psi \left(\dot{S} + \frac{1}{2m} (\nabla S)^2 \right) = \frac{\hbar^2}{2m} \square \psi + i\hbar \left(\dot{\psi} + \frac{1}{m} \nabla^\mu S \nabla_\mu \psi + \frac{1}{2m} (\square S) \psi \right). \quad (57)$$

Thus, we have the leading $\mathcal{O}(1)$ term producing the Hamilton–Jacobi equation for the eikonal phase S :

$$\dot{S} + \frac{1}{2m} (\nabla S)^2 = 0. \quad (58)$$

If we define the covector and vector fields as

$$p_\mu := \nabla_\mu S, \quad X^\mu := \frac{1}{m} \nabla^\mu S = \frac{1}{m} p^\mu, \quad (59)$$

and differentiate (58) covariantly we get

$$\partial_s p_\lambda + \frac{1}{2m} \nabla_\lambda (p^\mu p_\mu) = 0 \quad \implies \quad \partial_s p_\lambda + \frac{1}{m} p^\mu \nabla_\lambda p_\mu = 0. \quad (60)$$

Now $p_\mu = \nabla_\mu S$ is a gradient of a scalar, hence

$$\nabla_\lambda p_\mu = \nabla_\mu p_\lambda. \quad (61)$$

Using this relation in (60), substituting $p_\lambda = mX_\lambda$ (59), raising the index produces,

$$\partial_s X^\nu + X^\mu \nabla_\mu X^\nu = 0. \quad (62)$$

This is precisely the geodesic velocity equation (1). The numerical velocity fields displayed in Figure 2 are not of this eikonal-gradient special form; the discussion here is only a semiclassical comparison.

Now moving on to the next order $\mathcal{O}(\hbar)$ in (57), one obtains after imposing (58),

$$\dot{\psi} + X^\mu \nabla_\mu \psi + \frac{1}{2} (\nabla_\mu X^\mu) \psi = 0, \quad (63)$$

which is exactly the amplitude-flow equation (19). We can ignore the residual $\mathcal{O}(\hbar^2)$ term in this semiclassical analysis. Related WKBJ derivations of the Hamilton–Jacobi equation, the continuity equation for the leading amplitude density, and amplitude/spin transport along the associated mechanical trajectories were given by Stachel and Plebański [20].

APPENDIX B. RAYCHAUDHURI EQUATION FOR THE GEODESIC FLOW

Here we demonstrate the Raychaudhuri identity behind the divergence term appearing in amplitude flow equation (26). We start from the second identity in (6) of the Introduction about the result of convective derivative acting the divergence $\Theta := \nabla_\mu X^\mu$,

$$\frac{D\Theta}{Ds} = -(\nabla_\mu X^\nu)(\nabla_\nu X^\mu) - R_{\mu\nu}X^\mu X^\nu, \quad (64)$$

where we recall that the velocity fields are unit normalised $X^\mu X_\mu = -1$. To recover the standard form of Raychaudhuri equation, we introduce the spatial projector orthogonal to X ,

$$h_{\mu\nu} = g_{\mu\nu} + X_\mu X_\nu, \quad h^\mu{}_\nu = \delta^\mu{}_\nu + X^\mu X_\nu. \quad (65)$$

It satisfies $h_{\mu\nu}X^\nu = 0$ and has trace $h^\mu{}_\mu = 3$. The projected deformation tensor is

$$B_{\mu\nu} := h_\mu{}^\alpha h_\nu{}^\beta \nabla_\alpha X_\beta. \quad (66)$$

It is orthogonal to X in both indices and therefore acts as a 3×3 matrix on the local rest space perpendicular to the flow.

It is useful to keep track of the acceleration part,

$$a_\nu := X^\alpha \nabla_\alpha X_\nu, \quad (67)$$

which using $X^\nu \nabla_\mu X_\nu = 0$ from the unit-speed condition allows one to express the deformation tensor as,

$$B_{\mu\nu} = \nabla_\mu X_\nu + X_\mu a_\nu, \quad \implies \quad \nabla_\mu X_\nu = B_{\mu\nu} - X_\mu a_\nu. \quad (68)$$

In the quadratic term in (64), however, the acceleration contribution drops out:

$$(\nabla_\mu X^\nu)(\nabla_\nu X^\mu) = B_\mu{}^\nu B_\nu{}^\mu, \quad (69)$$

due to X -orthogonality, $B_{\mu\nu}X^\nu = X^\mu B_{\mu\nu} = 0$ and $X^\mu a_\mu = 0$.

We now decompose the spatial 3×3 tensor $B_{\mu\nu}$ into its trace, symmetric traceless, and antisymmetric parts:

$$B_{\mu\nu} = \frac{1}{3}\Theta h_{\mu\nu} + \sigma_{\mu\nu} + \omega_{\mu\nu}, \quad (70)$$

where

$$\Theta = B^\mu{}_\mu = \nabla_\mu X^\mu, \quad \sigma_{\mu\nu} = B_{(\mu\nu)} - \frac{1}{3}\Theta h_{\mu\nu}, \quad \omega_{\mu\nu} = B_{[\mu\nu]}. \quad (71)$$

The tensor $\sigma_{\mu\nu}$ is the shear and $\omega_{\mu\nu}$ is the vorticity. Using (70) into (69) we obtain

$$B_\mu{}^\nu B_\nu{}^\mu = \frac{1}{3}\Theta^2 + \sigma_{\mu\nu}\sigma^{\mu\nu} - \omega_{\mu\nu}\omega^{\mu\nu}. \quad (72)$$

Substituting this into (64) and using scalar conventions $\sigma^2 = \frac{1}{2}\sigma_{\mu\nu}\sigma^{\mu\nu}$ and $\omega^2 = \frac{1}{2}\omega_{\mu\nu}\omega^{\mu\nu}$, we obtain the known form of the Raychaudhuri equation, albeit with a convective derivative:

$$\frac{D\Theta}{Ds} = -\frac{1}{3}\Theta^2 - 2\sigma^2 + 2\omega^2 - R_{\mu\nu}X^\mu X^\nu. \quad (73)$$

In the special eikonal-gradient case (59) of Appendix A, one may simplify this equation further by writing

$$X_\mu = \frac{1}{m}\nabla_\mu S, \quad \nabla_\mu X_\nu = \frac{1}{m}\nabla_\mu \nabla_\nu S, \quad (74)$$

so that

$$\omega_{\mu\nu} = 0, \quad \Theta = \nabla_\mu X^\mu = \frac{1}{m}\square S, \quad (75)$$

implying a vanishing vorticity and divergence reducing to laplacian of the eikonal phase. Notice that the numerical velocity fields in this paper are not of this gradient

type, but we record this simplification in order to connect with the general theory behind the semiclassical eikonal limit. Moreover, in the Schwarzschild vacuum background $R_{\mu\nu} = 0$, leading to

$$\frac{D\Theta}{Ds} = -\frac{1}{3}\Theta^2 - 2\sigma^2 \leq 0, \quad (76)$$

meaning that the expansion scalar would not increase in time. We can solve this along the integral curve $\gamma^\mu(\tau)$ (42) where $\frac{D\Theta}{Ds} = \frac{d\Theta}{d\tau}$ when the shear is known and vorticity vanishes to obtain the real amplitude factor in the exact solution (43),

$$\psi(s, x) = \psi(0, \gamma(0)) \exp\left[-\frac{1}{2} \int_0^s \Theta(\tau, \gamma(\tau)) d\tau\right].$$

This gives the geometric meaning of the real amplitude factor in the exact solution: positive expansion attenuates the envelope, while focusing enhances it. This factor is real and positive, and therefore does not affect the reduced phase. The phase shift is instead determined by the angular foot-point of the backward integral curve, equivalently by the integral of X^θ in (5).

DECLARATIONS

Acknowledgements. KK was supported by DFG project grant 515782239. SM was supported by Leverhulme Trust project grant RPG-2024-177. The numerical computations involved use of high performance computing facilities at QMUL.

Data availability. No experimental data were created in this work. All supporting code and numerical data used to generate the figures are publicly available at [13].

Conflict of interest. The authors have no competing interests to declare that are relevant to the content of this article.

REFERENCES

- [1] Y. Aharonov and D. Bohm, Significance of electromagnetic potentials in the quantum theory, *Phys. Rev.* **115** (1959) 485–491.
- [2] J. Anandan, Gravitational and rotational effects in quantum interference, *Phys. Rev. D* **15** (1977) 1448–1457.
- [3] E. J. Beggs, Noncommutative geodesics and the KSGNS construction, *J. Geom. Phys.* **158** (2020) 103851.
- [4] E. J. Beggs and S. Majid, *Quantum Riemannian Geometry*, Grundlehren der mathematischen Wissenschaften **355**, Springer (2020).
- [5] E. J. Beggs and S. Majid, Quantum geodesic flows and curvature, *Lett. Math. Phys.* **113** (2023) 73.
- [6] E. J. Beggs and S. Majid, Quantum geodesics in quantum mechanics, *J. Math. Phys.* **65** (2024) 012101.
- [7] E. J. Beggs and S. Majid, Generally covariant quantum mechanics, *Lett. Math. Phys.* **116** (2026) 9.
- [8] E. J. Beggs and S. Majid, Klein–Gordon flow on FLRW spacetimes, *arXiv:2501.18295* [gr-qc] (2025).
- [9] M. V. Berry, Quantal phase factors accompanying adiabatic changes, *Proc. Roy. Soc. A* **392** (1984) 45–57.
- [10] R. Colella, A. W. Overhauser and S. A. Werner, Observation of gravitationally induced quantum interference, *Phys. Rev. Lett.* **34** (1975) 1472–1474.
- [11] J. S. Dowker, A gravitational Aharonov–Bohm effect, *Nuovo Cimento B* **52** (1967) 129–135.
- [12] M. A. Hohensee, B. Estey, P. Hamilton, A. Zeilinger and H. Müller, Force-free gravitational redshift: proposed gravitational Aharonov–Bohm experiment, *Phys. Rev. Lett.* **108** (2012) 230404.
- [13] K. Kumar and S. Majid, Mathematica codes for Geometric Aharonov–Bohm phase effect around a black hole, *Submitted to Notebook Archive*.
- [14] K. Kumar and S. Majid, Geodesic flows on a black-hole background, *arXiv:2603.03222* [gr-qc] (2026).

- [15] J. K. Lawrence, D. Leiter and G. Szamosi, A gravitational “Aharonov–Bohm” effect, *Nuovo Cimento B* **17** (1973) 113–121.
- [16] R. G. Littlejohn, The semiclassical evolution of wave packets, *Phys. Rep.* **138** (1986) 193–291.
- [17] C. Overstreet, P. Asenbaum, T. Kovachy, R. Notermans, J. M. Hogan and M. A. Kasevich, Observation of a gravitational Aharonov–Bohm effect, *Science* **375** (2022) 226–229.
- [18] G. Papini, Particle wave-functions in weak gravitational fields, *Nuovo Cimento B* **52** (1967) 136–141.
- [19] J. Stachel, Globally stationary but locally static space-times: a gravitational analog of the Aharonov–Bohm effect, *Phys. Rev. D* **26** (1982) 1281–1290.
- [20] J. Stachel and J. Plebański, Classical particles with spin. I. The WKBJ approximation, *J. Math. Phys.* **18** (1977) 2368–2374.
- [21] L. Stodolsky, Matter and light wave interferometry in gravitational fields, *Gen. Relativ. Gravit.* **11** (1979) 391–405.